View Article Online / Journal Homepage / Table of Contents for this issue
Dynamic Article Links

Lab on a Chip

Cite this: *Lab Chip*, 2012, **12**, 758

www.rsc.org/loc

PAPER

Published on 08 December 2011. Downloaded by UNIVERSITY OF CINCINNATI on 08/01/2014 20:44:35.

Reconfigurable virtual electrowetting channels†

Ananda Banerjee,[a] Eric Kreit,[b] Yuguang Liu,[a] Jason Heikenfeld[b] and Ian Papautsky*[a]

Received 2nd September 2011, Accepted 23rd November 2011
DOI: 10.1039/c2lc20842c

Lab-on-a-chip systems rely on several microfluidic paradigms. The first uses a fixed layout of continuous microfluidic channels. Such lab-on-a-chip systems are almost always application specific and far from a true "laboratory." The second involves electrowetting droplet movement (digital microfluidics), and allows two-dimensional computer control of fluidic transport and mixing. The merging of the two paradigms in the form of programmable electrowetting channels takes advantage of both the "continuous" functionality of rigid channels based on which a large number of applications have been developed to date and the "programmable" functionality of digital microfluidics that permits electrical control of on-chip functions. In this work, we demonstrate for the first time programmable formation of virtual microfluidic channels and their continuous operation with pressure driven flows using an electrowetting platform. Experimental, theoretical, and numerical analyses of virtual channel formation with biologically relevant electrolyte solutions and electrically-programmable reconfiguration are presented. We demonstrate that the "wall-less" virtual channels can be formed reliably and rapidly, with propagation rates of 3.5–3.8 mm s^{-1}. Pressure driven transport in these virtual channels at flow rates up to 100 μL min^{-1} is achievable without distortion of the channel shape. We further demonstrate that these virtual channels can be switched on-demand between multiple inputs and outputs. Ultimately, we envision a platform that would provide rapid prototyping of microfluidic concepts and would be capable of a vast library of functions and benefitting applications from clinical diagnostics in resource-limited environments to rapid system prototyping to high throughput pharmaceutical applications.

Introduction

Microfluidics permits transport, storage, and fluid manipulation in small volumes, and is the driving force behind the 'lab-on-a-chip' technologies. Conventional lab-on-a-chip platforms use structured microfluidic channel networks for transporting and confining liquids.[1] Glass and polymers are common substrate materials in these microfluidic devices, with fabrication procedures well established.[2,3] While numerous applications in medical diagnostics, chemical sensing, and environmental monitoring have been demonstrated, any change in the design of these devices, regardless of how minute, requires a repeat of the entire fabrication cycle.

Programmable microfluidic devices have the potential to be reconfigured during operation. Digital microfluidic systems exhibit such functionality and are able to manipulate discrete sample volumes (droplets) on demand. Such systems have been demonstrated in a variety of lab-on-a-chip applications using electrowetting transport,[4–6,7] dielectrophoresis[8,9] and electrohydrodynamic forces.[10–12] However, while droplet manipulation is a critical capability, it cannot replace the functionalities provided by continuous microfluidics which enables processing of large sample volumes at high throughput. Attempts to demonstrate programmable continuous microchannels have been recently reported using surface energy[13] and microvalves.[14,15] While these early devices provide continuous flow, they offer very limited re-configurability. A truly reconfigurable continuous microfluidic system, in essence the merging of the two paradigms of continuous and digital microfluidics, would permit wide range of microfluidic functions in a wide range of applications ranging from clinical diagnostics in resource-limited environments to rapid system prototyping to high throughput pharmaceutical applications.

In this work, we demonstrate for the first time programmable formation of virtual microfluidic channels, as well as their continuous operation and reconfiguration with pressure driven flows using an electrowetting platform. In our earlier work, we demonstrated directional formation of virtual channels bounded by polymer post arrays[16] and showed that electrowetting channels can be made to retain their geometry in the absence of external stimulus using Laplace barriers.[17] Fig. 1 illustrates the

[a]*BioMicroSystems Laboratory, School of Electronic and Computing Systems, University of Cincinnati, 814 Rhodes Hall, ML030, Cincinnati, OH, 45221, USA. E-mail: ian.papautsky@uc.edu; Fax: +(513) 556-7326; Tel: +(513) 556-2347*
[b]*Novel Devices Laboratory, School of Electronic and Computing Systems, University of Cincinnati, Cincinnati, OH, 45221, USA*
† Electronic supplementary information (ESI) available. See DOI: 10.1039/c2lc20842c

This journal is © The Royal Society of Chemistry 2012

Published on 08 December 2011. Downloaded by UNIVERSITY OF CINCINNATI on 08/01/2014 20:44:35.

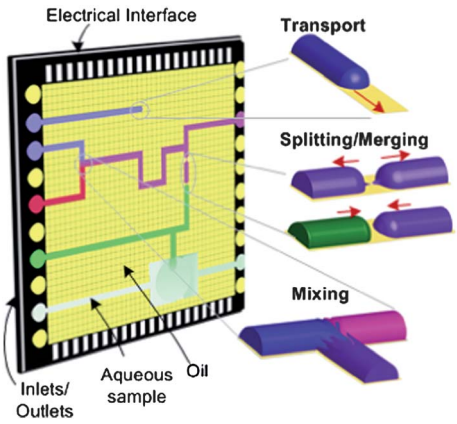


Fig. 1 Microfluidic platform based on electrowetting, integrating continuous and digital paradigms. Insets show sample transport, splitting and merging of channels and mixing of samples. Transparent conducting front plate (not shown) is grounded.

overall concept of our platform. It consists of an electrically-programmable two-dimensional array of insulated electrodes on the bottom plate. The transparent top plate is conductive and it is separated from the bottom plate by a spacer layer. This arrangement is used to form a sealed cavity with inlet and outlet ports. The capability of selectively applying potential to each electrode combined with sample injection using syringe pumps at the inlets makes it possible to demonstrate a variety of basic fluid manipulation and handling capabilities including, splitting and merging of microfluidic channels, mixing and sample transport in a programmable manner. The platform relies on electrowetting contact angle modulation of conducting aqueous samples in oil ambient over insulated electrodes, to define channel boundaries. Thus, in this work, first we considered biologically-relevant electrolytes at various pH values for the formation of our reconfigurable channels. Using the data obtained from these tests, we present a theoretical model for electrowetting channel formation, supported by experiments and numerical simulations. We extend this knowledge of channel formation to demonstrate reconfiguration of virtual electrowetting channels by incorporating electrically-controlled functions such as splitting and merging. While digital microfluidics[4] relies only on droplet manipulation, our platform permits channel formation of desired geometries 'on-demand' that can sustain pressure driven flows.

Device fabrication

Devices were fabricated using 1′x 3′ glass slides as the bottom substrate. The construction of the device is schematically represented in Fig. 2. A thin 200 nm layer of gold over 10 nm tungsten seed layer was evaporated over a glass slide. The metal layer was then patterned using photolithography to define the electrodes and the electrical connections. The metal electrodes were then coated with a layer of 1 μm thick Parylene-C (Speciality Coating Systems). A spacer layer was patterned using a negative photoresist (PerMX 3050, DuPont). This defined the height of the virtual channels (100 μm) and boundaries of the inlet and outlet ports as shown in Fig. 2. The inlet and outlet ports were confined at the back end and at the front end respectively to restrict the conducting fluid from moving into undesired areas of the chip. A glass slide with a conductive layer of $In_2O_3 : SnO_2$ (ITO) was used as a top cover. The top cover is drilled at the inlet and outlet locations using diamond coated drill bits. Both the bottom and the top substrates were coated with a thin (50 nm) layer of hydrophobic fluoropolymer (Cytonix Fluoropel 1601V). This ensured that the conducting liquid has a contact angle (Young's angle) of 180° without an applied voltage. Next, the top and bottom substrates are bonded together using an UV-curable epoxy, ensuring that the device is sealed on all sides except at the inlet and the outlet. Ferrules are epoxy-glued over the inlet/outlet holes on the top plate to attach tubing that carries ambient oil (OS-30, Dow Corning) and the conducting fluid sample.

Electrowetting characterization of electrolytes

Electrolyte solutions and buffers of various ionic strengths and pH are widely used in biochemical analyses. Droplet microfluidics has been used to demonstrate diagnostic lab-on-chip, capable of processing biological samples including saliva, urine, blood and buffer solutions.[18,19] Ultimately, we envision using our platform in similar applications. Thus, we first considered several of the commonly used electrolytes including phosphates, acetates and chlorides for preparing the conductive fluid. To characterize these biologically-relevant electrolyte solutions, we have used an arrangement illustrated in Fig. 3. The metal layer was connected to a DC power supply and the setup was immersed in an oil bath filled with OS-30 oil. A droplet of electrolyte solution was carefully placed over the hydrophobic dielectric surface and a thin tungsten wire was inserted in it to provide the ground connection. Electrowetting contact angle modulation was performed by varying the applied voltage at the metal layer. The applied voltage (V) is related to the *apparent* contact angle[20,21] θ_V by the Young-Lippmann equation[6,22]

$$cos\theta_V = cos\theta_Y + V^2(\varepsilon_0\varepsilon/2\gamma_{ci}t) \quad (1)$$

where θ_Y is the contact angle at $V = 0$ V, $\varepsilon_0 = 8.854 \times 10^{-12}$ is the permittivity of free space, $\varepsilon = 3.15$ is the relative permittivity of the Parylene C dielectric layer,[23,24] t is dielectric layer thickness, and γ_{ci} is the interfacial tension between the conducting and insulating fluids. On a hydrophobic dielectric, where the Young's angle θ_Y is approximately 180°, the contact angle θ_V can be modulated down to 45∼60° by applying voltage suitably, before contact angle saturation occurs.

We have characterized the electrowetting contact angle modulation for several biologically relevant electrolytes including, monosodium phosphate ($NaH_2PO_4 \cdot 7H_2O$), sodium acetate (CH_3COONa) and sodium chloride (NaCl) at near neutral pH values (6–8). The data from these experiments are presented in Fig. 4. Using these data, we estimated the value of the interfacial tension between the electrolyte droplet and the insulating oil (γ_{ci}) in each case and used the Young-Lippmann equation (eqn (1)) to plot the theoretical trend. This trend analysis was performed for all three electrolytes at a concentration of 100 mM. The experimental data agree with the Young-Lippmann curves within ±3°, until contact angle saturation occurs. The Young-Lippmann model does not account for this saturation[25] and the physical origins of this phenomenon have

Published on 08 December 2011. Downloaded by UNIVERSITY OF CINCINNATI on 08/01/2014 20:44:35.

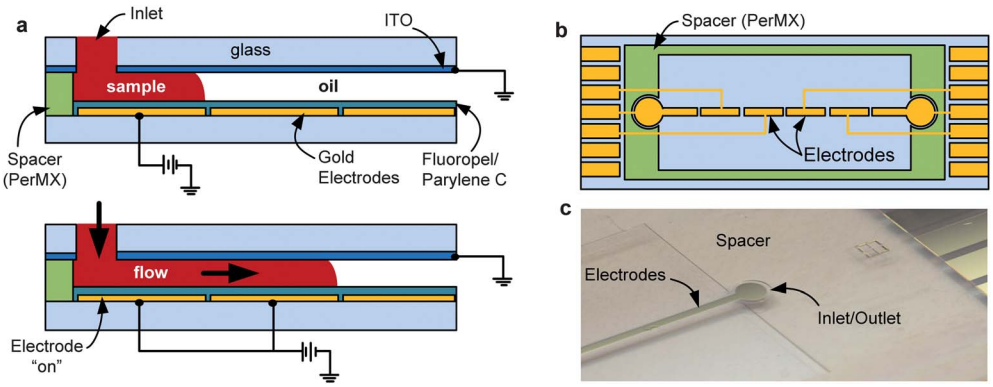


Fig. 2 (a) Cross-section of a pressure driven electrowetting device. A virtual microfluidic channel forms when potential is applied to gold electrodes and sample is injected at the inlet. (b) Top view of a single channel device illustrating the layout of electrodes and the spacer layer (PerMX photoresist). (c) Photograph of device illustrating the bottom plate with gold electrodes and the spacer layer at an inlet/outlet port. The spacer layer is 100 μm in thickness and defines height of the virtual channel.

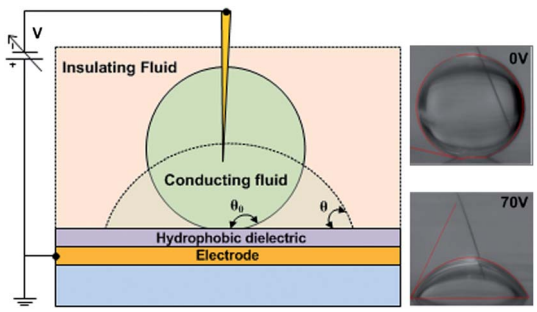


Fig. 3 Electrowetting on dielectric test setup. The electrode is gold; the hydrophobic dielectric layer consists of 1 μm thick Parylene-C coated with 50 nm of Fluoropel. When potential $V = 0$V, the contact angle is θ_0 (Young's Angle). When the potential is increased to a higher value, the contact angle modulates down to θ. A droplet of phosphate electrolyte undergoing contact angle modulation is shown on the right.

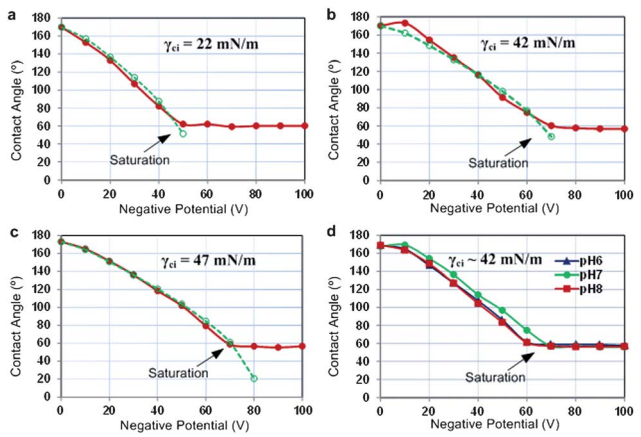


Fig. 4 Electrowetting characteristic for 100 mM (a) sodium phosphate, (b) sodium acetate, and (c) sodium chloride solutions. Dashed lines represent theoretical values obtained from the Young-Lippmann equation (interfacial tension between conducting and insulating liquids (γ_{ci}) is estimated as indicated). Solid lines show the experimental data. (d) Electrowetting characteristic of sodium acetate electrolyte solution at pH 6, 7 and 8. Contact angle saturation occurs below 70 V for all samples.

not yet been explained successfully. The experimental data for electrowetting characterization of sodium acetate solutions at near neutral pH values indicates that pH does not have a significant effect on electrowetting modulation, which is in agreement with the recent work on contact angle saturation.[25]

As indicated by the data, in our electrowetting setup all of the tested electrolytes start exhibiting contact angle saturation at or below 70 V. We thus chose this value as the operating point for all our experiments to ensure that all the tested samples undergo maximum contact angle modulation in our devices. We used phosphate electrolyte solution of 100 mM concentration as the conducting fluid in this work because of its lower saturation potential as compared with other electrolytes.

Model of virtual channel formation

To form a virtual channel on an electrowetting on dielectric (EWOD) platform, electric potential must be applied to adjacently placed, insulated electrodes such that the activated electrodes form a straight path of defined length and width. A microchannel is drawn over the electrodes when an electrolyte is injected through the inlet port over the first voltage-activated electrode. The conducting electrolyte electrowets the surface of the dielectric wherever potential is applied which lowers the apparent contact angle between the dielectric surface and the conducting medium. If the electrolyte is pumped into a device initially filled with insulating oil, it will conform to the shape of the activated electrodes and displace an equal volume of oil, thus forming a virtual channel.

The voltage-activated electrodes define a continuous path between the inlet and the outlet, over which the injected electrolyte propagates. Fig. 5 illustrates the propagating meniscus of such a virtual microchannel with side panels illustrating top and cross-sectional views. If the Laplace pressure[6] on the front of the meniscus is assumed to be the same as pressure on the side of the propagating channel, the advancing meniscus pressure can be calculated as

$$\Delta p = \gamma_{ci}\,(1/R_h + 1/R_v) \qquad (2)$$

 This journal is © The Royal Society of Chemistry 2012

Published on 08 December 2011. Downloaded by UNIVERSITY OF CINCINNATI on 08/01/2014 20:44:35.

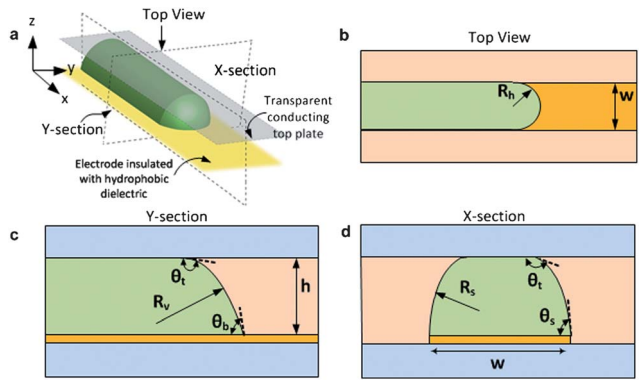


Fig. 5 Schematic illustration of a virtual channel. (a) Conducting liquid forming a channel over an electrode-strip. (b) Top-view showing horizontal radius of curvature of the front of the meniscus and straight side-boundaries of the virtual channel. (c) Y-section depicting the horizontal radius of curvature and top and bottom contact angles of the front of the meniscus. (d) X-section showing the vertical radius of curvature of the side boundaries of the channel and the top and bottom contact angles of the meniscus on the channel sides.

where R_h and R_v represent the horizontal and vertical radii of curvature of the front meniscus. From the channel geometry, the horizontal radius of curvature is assumed to be approximately half the width (w) of the channel ($R_h = w/2$). For the case of confinement between the top and bottom plates separated by a height (h), the vertical radius of curvature is given by

$$R_v = -h/(cos\theta_t + cos\theta_b) \quad (3)$$

where θ_t and θ_b are the contact angles on the top and bottom plates respectively. Although our results (Fig. 4) show contact angle ~170° at an applied voltage of 0 V, the microscopic contact angle, which is not observable in our setup is expected to be closer to 180° (the Young's angle) since the top plate is coated with a hydrophobic fluoropolymer and is grounded. For simplicity of analysis we will assume that this angle is $\theta_t \sim 180°$. On the bottom plate, the contact angle is modulated to $\theta_b \sim 60°$ by the applied voltage. Using these parameters, the Laplace pressure at the front of the meniscus can then be expressed as

$$\Delta p_{front} = \gamma_{ci}\,(2/w + 1/(2h)) \quad (4)$$

For the sides of the channel, the vertical radius of curvature is denoted as R_s and the contact angle on the bottom is represented by θ_s (Fig. 5d). Looking from the top, the side of the channel is straight; therefore the horizontal radius of curvature is infinite. Using these parameters, we obtain the expression for the Laplace pressure for the side from eqn (2) and the expression for the vertical radius of curvature of the sides of the channel from eqn (3) as

$$\Delta p_{side} = \gamma_{ci}/R_s \quad (5)$$

$$R_s = h/(1-cos\theta_s) \quad (6)$$

Since the Laplace pressure on the sides of the microchannel must equate the Laplace pressure at the front, equating eqn (4) and eqn (5) yields the value for R_s as

$$R_s = 2hw/(4h + w). \quad (7)$$

The corresponding value of θ_s can be determined from eqn (6) as

$$\theta_s = \cos^{-1}\left(\frac{w - 4h}{2w}\right) \quad (8)$$

In our experiments, the width of the electrode was $w = 500$ μm and the height of the channel (separation between top and bottom substrates) was $h = 100$ μm. For these conditions, the side radius of curvature is calculated to be $R_s \sim 111$ μm, while the side contact angle at the bottom is calculated to be $\theta_s \sim 84°$.

From the above theoretical discussion we can see that the bottom plate contact angle at the sidewalls of the virtual microchannel is larger than the contact angle at the front of the meniscus ($\theta_s > \theta_b$), which indicates bulging at the sidewalls. When a small volume of electrolyte is pumped into the channel, the channel boundary bulges slightly on the sides, resulting in a change in the apparent contact angle at the bottom plate. This disrupts the equilibrium condition such that the Laplace pressure from the sides becomes larger than the Laplace pressure at the front of the channel. To equilibrate pressures and relieve the sidewall bulge, the front meniscus of the channel must propagate forward over the electrode. In this manner, the liquid forms a continuous virtual channel by propagating over available activated electrodes, as long as the fluid is introduced at the inlet.

For a device consisting of a single inlet and a single outlet, once a microchannel is established by propagation over an activated path from the inlet to the outlet, the electrolyte can be continuously pumped at the desired flow rate. This continuous operation of these virtual "wall-less" channels with a syringe pump is similar to pressure driven flows in microfluidic channels with rigid channel boundaries. However, the geometry of the channel in this case is programmable and may be changed during the operation of the device, simply by applying potential to electrodes.

The theoretical model of channel formation was confirmed using numerical simulations in CFD-ACE+ (ESI Inc.). The modeled straight channel was 500 μm in length, 100 μm in height and 500 μm in width. Flow module and free surface module (VOF) were used to introduce a secondary liquid into a primary liquid, to realize an immiscible fluid-fluid interface. The primary liquid was defined as OS-30 oil and the secondary liquid was defined to be an electrolyte solution. The activated electrode was defined by a static wetting angle of 60°, while all the deactivated areas had a wetting angle of 180°. The choice of these values is consistent with the electrowetting characteristics of phosphate electrolyte solution of 100 mM concentration. In CFD-ACE+, the surface reconstruction method determines how the secondary fluid flows into the primary fluid. In our case, Piecewise Linear Interface Construction (PLIC) was used. Auto time step was used in the simulation, with the initial time step set as 1 μs to accommodate the minimum cell size and reach a satisfactory convergence of all residuals to less than 10^{-4}. Fig. 6 illustrates the simulation results. The shape of the front meniscus and its radius of curvature match our theoretical model closely. The horizontal radius curvature of the front meniscus was predicted to be $R_h \sim 250$ μm (Fig. 6b), confirming our assumption in the theoretical analysis. The vertical radius of curvature was measured

Published on 08 December 2011. Downloaded by UNIVERSITY OF CINCINNATI on 08/01/2014 20:44:35.

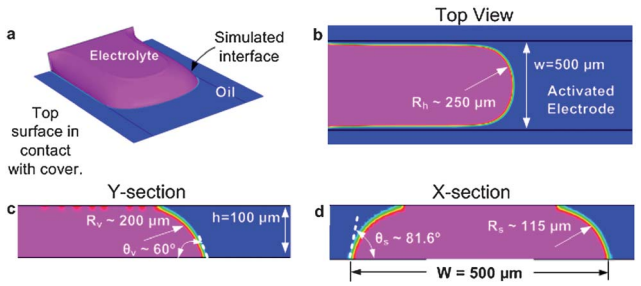


Fig. 6 (a) CFD-ACE+ model of a propagating electrolyte meniscus (virtual channel) in oil. (b) Top view of simulated model indicating the horizontal radius of curvature of the front meniscus. (c) Y-section view of the simulated virtual microchannel. The simulated values of the vertical radius of curvature and bottom contact angle at the front of the meniscus are shown. (d) X-section view illustrating the sides of the channel indicating the radius of curvature of the sidewalls and the bottom contact angle at the sides.

from the simulated model to be $R_v \sim 200$ μm and the bottom contact angle at the front meniscus to be $\theta_b \sim 60°$ (Fig. 6c). The simulation also predicted the contact angle at the side to be $\theta_s \sim 81.6°$ and the sidewall radius curvature, to be $R_s \sim 116$ μm. These results confirm our theoretical model within tolerable error limits.

Demonstration of virtual channel formation

Next, we experimentally demonstrated formation of virtual microchannels. A device consisting of electrodes configured to form a virtual channel 3 cm in length is illustrated in Fig. 7a. A power-supply set to provide square wave output at 70 V (RMS) at 100 Hz was connected through a switch box. The ITO layer at the bottom of the top plate was grounded as indicated. Once the device was completely filled with oil, the voltage was turned on and the device was ready to receive the electrolyte. The electrolyte solution (100 mM sodium phosphate) was colored red using pigment dispersion (Sun Chemical). This fluid was pumped in at a continuous flow rate of 10 μL min^{-1}.

A magnified image of the propagating meniscus of the conducting (red) fluid during virtual channel formation is shown in Fig. 7b. The horizontal radius of curvature of this meniscus is clearly half channel width, measured be $R_h \sim 250$ μm which agrees with our modeling results (Fig. 6b) and the assumption made in the theoretical analysis (Fig. 5b). The front of the meniscus exhibits visible fading when viewed from the top, indicating a thinner fluid due to electrowetting of the meniscus at the bottom down to $\theta_b \sim 60°$. The sidewalls of the channel appear relatively sharp and straight, which is expected since the sidewall contact angle θ_s is quite vertical, 82–84° from the theoretical analysis and the numerical model. These results substantiate our theory of virtual channel formation.

The straight virtual channel forms over the activated electrode at a continuous flow rate as indicated by the time lapsed images in Fig. 7c. As more fluid is pumped in, the excess volume of oil inside the sealed cavity of the device drains out through the outlet. The rate of formation of the channel was measured from the time lapsed images to be ~3.5 mm s^{-1}, which is slightly less than the prediction by our simulation (3.8 mm s^{-1}). The propagation rate can also be estimated from the input flow rate ($Q = 10$ μL min^{-1}) and the hydraulic diameter D_h of the virtual channel ($D_h = 4A/P$, where A is the cross-section area and P is the perimeter). From the cross-sectional parameters calculated by eqn (7) and (8), the hydraulic diameter of our virtual channel is $D_h \sim 162$ μm, which yields the channel propagation velocity of ~3.7 mm s^{-1}. Overall, the experimental results are in reasonable agreement with our numerical and theoretical predictions. Fig. 7d illustrates continuous pumping through a capillary tube connected at the outlet.

Continuous operation of our virtual channels is a two-step process. The device by itself is a sealed cavity with operational inlets and outlets. The first step is to form the virtual channel which proceeds with the introduction of conducting fluid through the inlet and the consequent displacement of oil through the outlet. The velocity of channel formation is a function of the flow rate at which fluid is introduced at the inlet, and the channel dimensions. The flow rate can be adjusted to obtain the desired velocity for a given channel dimension. However, we have observed that high rate of formation of virtual channels leads to unpredictable bulging of the channel near the inlet and spreading of the conducting fluid into undesired areas of the chip. The maximum rate of channel formation is a parameter that we will optimize in future work. We also note that air bubble introduction and aqueous droplet formation are practical concerns

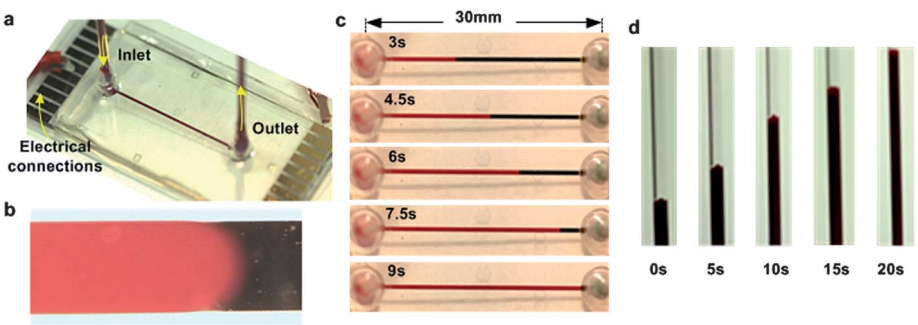


Fig. 7 (a) A virtual microfluidic device, illustrating formation of a 30 mm long straight channel. Conducting liquid is phosphate electrolyte solution (100 mM) colored with red pigment dispersion. Flow rate of 10 μL min^{-1} was maintained at the inlet using a syringe pump. (b) Magnified image of the propagating meniscus, showing relatively straight side walls (single line) and gradient at the front of the meniscus. (c) Time Lapsed images (stills from video) of channel formation. Refer to ESI for videos. (d) Rise of liquid meniscus in a capillary tube connected at outlet shows continuous transport through the virtual channel.

 This journal is © The Royal Society of Chemistry 2012

Published on 08 December 2011. Downloaded by UNIVERSITY OF CINCINNATI on 08/01/2014 20:44:35.

that we have considered. The aqueous sample follows the oil through the same inlet to avoid introduction of air bubbles. We do occasionally observe aqueous droplets when we flush the device with oil to erase channel pattern and reintroduce aqueous samples to form a new channel. Nevertheless, these droplets typically become trapped at the corners of the sealed cavity of the device (next to the spacer layer) and do not interfere with device operation.

The second step is continuous pressure driven transport through the formed virtual channel. After successfully connecting a conducting liquid conduit from the inlet to the outlet, the oil has no path to exit the device because of the edge seal. This ensures that the device can be continuously operated at high flow rates without deforming the boundaries of the channel. The maximum rate at which a virtual channel can be formed is smaller than the rate at which the channels can be continuously operated. Fig. 7d illustrates continuous pumping through a capillary tube connected at the outlet. The meniscus rises at a constant rate. We have successfully tested flow rates as high as 100 μL min^{-1} without deforming the boundaries of the channel.

Demonstration of reconfiguration of virtual channels

The idea of forming straight channels by activating electrodes in a straight path can be extended to form channels with non-linear geometry. However, to reconfigure the geometry of the flow path it is necessary to first establish the capability of splitting and merging electrowetting channels. The mechanism is similar to that of droplet splitting and merging.[5] In this work, we demonstrate this operation using a three electrode configuration, where the middle electrode is switched off to achieve splitting. Devices were fabricated using the same procedure as described earlier. Instead of a single electrode however, several closely-spaced electrodes were adjacently laid out and activated to form a straight liquid conduit, by pumping electrolyte from an inlet. The flow was stopped when the channel had formed completely connecting the inlet to the outlet. To achieve splitting of the channel, a 4 mm long electrode segment was deactivated. Fig. 8a illustrates splitting of a virtual channel. In this case, the deactivated strip was preceded by a longer fluid conduit (towards the inlet). The conduit of fluid succeeding it is shorter in length. It was observed that necking starts to occur on the non-energized strip near the succeeding end, so that the larger fluid conduit retains most of fluid when the splitting is complete. Importantly, both fluid conduits gain a certain volume of fluid that was earlier occupying the electrode strip. This leads to a certain amount of bulging. Since the Laplace pressure at the sidewalls of both fluid segments must be equal at the instance of the splitting, it occurs in a way such that both conduits of fluid bulge by the same amount and the longer conduit of fluid can accommodate a larger volume of fluid by undergoing the same amount of bulge at its side walls as the smaller conduit of fluid.

We have also demonstrated merging of two liquid conduits using the same experimental setup. Fig. 8b illustrates two approaching menisci. The same electrode that was deactivated to effect splitting was turned back on, which resulted in the liquid being pulled back into the activated electrode. The menisci approach and merge to reform a single conduit.

A combination of the functions of formation, transport, splitting and merging can be used to define channels of desired geometry connecting several inlets to several outlets. Virtual microfluidic channels designed for a particular function can be formed in a programmable fashion, by appropriately biasing electrodes and maintaining a supply of conducting fluid. In conventional microfluidic devices with channels of fixed geometries, active or passive valves are used for switching fluidic pathways. In contrast, virtual microfluidic channels can be re-routed or reconfigured to select one or more of several possible fluidic pathways for transport between inlets and outlets. The functionality provided by active or passive valves on a microfluidic channel of fixed geometry, is achieved by splitting and merging channels in a programmable fashion by appropriately activating or deactivating certain electrodes.

As a proof of this concept of programmable channel formation and reconfiguration of fluidic pathways, we demonstrate a device with a pair of inlets and outlets in the form of an 'X' channel. Fig.9 illustrates the various fluidic pathways that we tested. One or both inlets ('A' and 'B') could be selectively connected through a straight channel to one or both outlets ('C' and 'D'). The flow rate at each inlet was maintained at 5 μL min^{-1}. The virtual

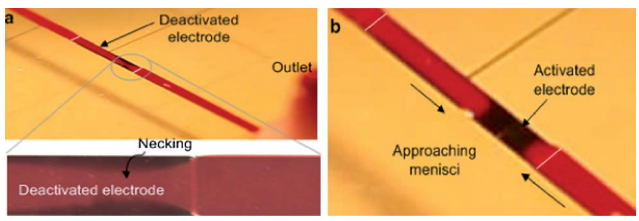


Fig. 8 (a) Photograph of device, showing splitting. Close-up of deactivated electrode shows necking (b) Merging of two approaching menisci. White lines are used to mark the boundaries of the electrodes.

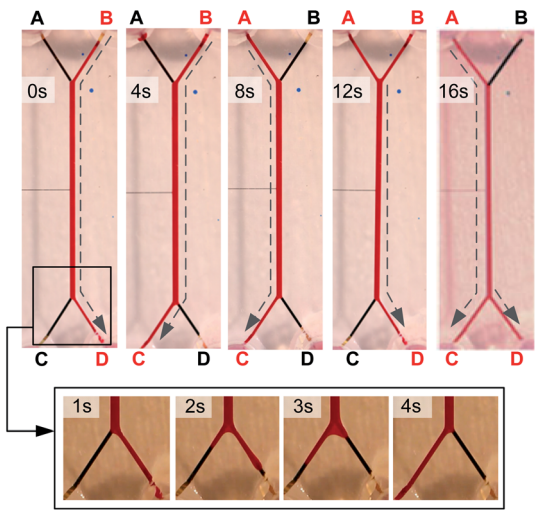


Fig. 9 Programmable fluid paths in an 'X-channel'. Each inlet (top) and outlet (bottom) can be activated independently by application of bias to the associated electrode. Channel formation from top to bottom: B to D, B to C, A to C, A&B to D, and A to C&D. Flow rate at each inlet was maintained at 5 μL min^{-1}. Insets illustrate transition from outlet D to C. The virtual microchannel recedes when outlet D is deactivated (1s) and reforms when outlet C is activated (3s). Refer to ESI for videos.

Published on 08 December 2011. Downloaded by UNIVERSITY OF CINCINNATI on 08/01/2014 20:44:35.

channel was first formed between inlet 'B' and outlet 'D' by activating corresponding electrodes. The straight electrode strip in middle always stays on. Then, the electrode corresponding to outlet 'D' was switched off and the electrode corresponding to outlet 'C' was switched on. This resulted in a splitting of the channel over 'D', followed by formation of a new channel over 'C', defining a new path as illustrated by the insets (Fig. 9). The splitting in this case occurs close to the outlet reservoir of 'D'. This is because the outlet reservoir is completely filled and has no room to bulge. The straight channel in the middle is the larger body of fluid and can accommodate the volume previously occupied by the channel over 'D'. When the electrode corresponding to 'C' is turned on, the bulge in the straight channel is relieved by the propagation of the meniscus over the electrode. In a similar fashion we could reconfigure the channel to obtain the different fluidic pathways as illustrated. The switching of fluidic pathways between outlets could be performed while fluid was still being pumped. When a particular inlet needed to be activated or deactivated, the syringe pump connected to it had to be turned on or off appropriately, accompanied by the application of the voltage at the necessary electrodes.

Conclusions

Programmability in microfluidic channels allows wider access to multiple microfluidic functions. Modular microfluidic breadboards[14] adopt a scheme where separate interconnections are manufactured for each application. This allows for a certain level of abstraction to access specific microfluidic functions. General purpose microfluidic chips have also been reported recently.[26] However, geometries form the basis of many continuous microfluidic applications. True programmability in a microfluidic platform can be realized when specific *geometries* can be defined by the user, suiting the needs of a particular application. Provision for the processing of discrete sample volumes and precise control of sample metering should also be built into such a platform.

Droplet manipulation has been widely discussed in both rigid channels as well as in electrowetting based multiphase fluidic systems. EWOD based microfluidic platforms[4,5] have become popular in the recent years due to their inherent capability to be programmable. While digital microfluidics allows for a certain degree of computer control of functions, they are limited by small sample volumes and non-continuous operation. The integration of continuous microfluidic functions on an electrowetting based platform would lead to the merging of the two paradigms of continuous microfluidics and droplet based digital microfluidics, allowing for a much wider range of functionality and possible applications.

A microfluidic platform capable of on-demand formation of microchannels of desired geometries can take advantage of the vast library of applications that have been developed using continuous microfluidics over the years. In this work, we developed a model of virtual channel formation and demonstrated the most critical basic functions such as pressure driven transport and switching of programmable fluidic pathways. At this stage we used metal electrodes to define our geometries. In the future, however, we envision using an array of smaller, individually-addressable electrodes, such as active matrix drive, to achieve any desired geometry. Such programmability would move us beyond today's 'instrument'-on-chip, and lead to a new class of 'laboratory'-on-a-chip systems. Such an agile lab-on-chip would allow access to a large library of laboratory tasks, but with portability and user-control similar to that of a reconfigurable integrated circuit such as a field-programmable gate array (FPGA), and perhaps ultimately similar to a smart phone.

Acknowledgements

We gratefully acknowledge support by the National Science Foundation (ECCS-1001141) and the Defense Advanced Research Projects Agency (DARPA) N/MEMS S&T Fundamentals Program under grant no. N66001-1-4003 issued by the Space and Naval Warfare Systems Center Pacific (SPAWAR) to the Micro/nano Fluidics Fundamentals Focus (MF3) Center.

References

1 G. M. Whitesides, *Nature*, 2006, **442**, 368–373.
2 S. K. Sia and G. M. Whitesides, *Electrophoresis*, 2003, **24**, 3563–3576.
3 J. W. Hong and S. R. Quake, *Nat. Biotechnol.*, 2003, **21**, 1179–1183.
4 R. B. Fair, *Microfluid. Nanofluid.*, 2007, **3**, 245–281.
5 S. K. Cho, H. Moon and C. J. Kim, *J. Microelectromech. Syst.*, 2003, **12**, 70–80.
6 J. Berthier, in *Micro-Drops and Digital Microfluidics*, ed. J. Ramsden, William Andrew Publishing, Norwich, NY, 2008, pp.7–73.
7 D. Chatterjee, H. Shepherd and R. L. Garrell, *Lab Chip*, 2009, **9**, 1219–1229.
8 P. R. C. Gascoyne, J. V. Vykoukal, J. A. Schwartz, T. J. Anderson, D. M. Vykoukal, K. W. Current, C. McConaghy, F. F. Becker and C. Andrews, *Lab Chip*, 2004, **4**, 299–309.
9 T. P. Hunt, D. Issadore and R. M. Westervelt, *Lab Chip*, 2007, **8**, 81–87.
10 O. D. Velev, B. G. Prevo and K. H. Bhatt, *Nature*, 2003, **426**, 515–516.
11 J. Zeng and T. Korsmeyer, *Lab Chip*, 2004, **4**, 265–277.
12 M. A. Burns, B. N. Johnson, S. N. Brahmasandra, K. Handique, J. R. Webster, M. Krishnan, T. S. Sammarco, P. M. Man, D. Jones, D. Heldsinger, C. H. Mastrangelo and D. T. Burke, *Science*, 1998, **282**, 484–487.
13 B. Zhao, J. S. Moore and D. J. Beebe, *Science*, 2001, **291**, 1023–1026.
14 K. A. Shaikh, K. S. Ryu, E. D. Goluch, J. M. Nam, J. Liu, C. S. Thaxton, T. N. Chiesl, A. E. Barron, Y. Lu, C. A. Mirkin and C. Liu, *Proc. Natl. Acad. Sci. U. S. A.*, 2005, **102**, 9745–9750.
15 L. M. Fidalgo and S. J. Maerkl, *Lab Chip*, 2011, **11**, 1619.
16 M. Dhindsa, J. Heikenfeld, S. Kwon, J. Park, P. D. Rack and I. Papautsky, *Lab Chip*, 2010, **10**, 832–836.
17 E. Kreit, M. Dhindsa, S. Yang, M. Hagedon, K. Zhou, I. Papautsky and J. Heikenfeld, *Langmuir*, 2010, **26**, 18550–18556.
18 V. Srinivasan, V. K. Pamula and R. B. Fair, *Anal. Chim. Acta*, 2004, **507**, 145–150.
19 V. Srinivasan, V. K. Pamula and R. B. Fair, *Lab Chip*, 2004, **4**, 310–315.
20 J. B. F. Mugele, *J. Phys.: Condens. Matter*, 2007, **19**, 375112.
21 R. Gupta, G. K. Olivier and J. Frechette, *Langmuir*, 2010, **26**, 11946–11950.
22 M. G. Lippmann, *Ann. Chim. Phys*, 1875, **1**, 494.
23 M. Dhindsa, J. Heikenfeld, W. Weekamp and S. Kuiper, *Langmuir*, 2011, **27**, 5665–5670.
24 Y. Y. Lin, R. D. Evans, E. Welch, B. N. Hsu, A. C. Madison and R. B. Fair, *Sens. Actuators,B*, 2010, **150**, 465–470.
25 S. Chevalliot, S. Kuiper and J. Heikenfeld, *J. Adhes. Sci. Technol*, 2011, DOI: 10.1163/156856111X599580.
26 J. P. Urbanski, W. Thies, C. Rhodes, S. Amarasinghe and T. Thorsen, *Lab Chip*, 2006, **6**, 96–104.

 This journal is © The Royal Society of Chemistry 2012